



Kinetically Stable Oxide Overlayers on Mo₃P Nanoparticles Enabling Lithium–Air Batteries with Low Overpotentials and Long Cycle Life

Alireza Kondori, Zhen Jiang, Mohammadreza Esmaeilirad, Mahmoud Tamadoni Saray, Arvin Kakekhani, Kamil Kucuk, Pablo Navarro Munoz Delgado, Sadaf Maghsoudipour, John Hayes, Christopher S. Johnson, Carlo U. Segre, Reza Shahbazian-Yassar, Andrew M. Rappe, and Mohammad Asadi*

The main drawbacks of today's state-of-the-art lithium–air (Li–air) batteries are their low energy efficiency and limited cycle life due to the lack of earth-abundant cathode catalysts that can drive both oxygen reduction and evolution reactions (ORR and OER) at high rates at thermodynamic potentials. Here, inexpensive trimolybdenum phosphide (Mo₃P) nanoparticles with an exceptional activity—ORR and OER current densities of 7.21 and 6.85 mA cm⁻² at 2.0 and 4.2 V versus Li/Li⁺, respectively—in an oxygen-saturated non-aqueous electrolyte are reported. The Tafel plots indicate remarkably low charge transfer resistance—Tafel slopes of 35 and 38 mV dec⁻¹ for ORR and OER, respectively—resulting in the lowest ORR overpotential of 4.0 mV and OER overpotential of 5.1 mV reported to date. Using this catalyst, a Li–air battery cell with low discharge and charge overpotentials of 80 and 270 mV, respectively, and high energy efficiency of 90.2% in the first cycle is demonstrated. A long cycle life of 1200 is also achieved for this cell. Density functional theory calculations of ORR and OER on Mo₃P (110) reveal that an oxide overlayer formed on the surface gives rise to the observed high ORR and OER electrocatalytic activity and small discharge/charge overpotentials.

The advancement of lithium–air (Li–air) batteries, proposed as a potential alternative for existing energy storage systems, is mainly hampered by low energy efficiency and limited cycle life. One of the major drawbacks for today's Li–air batteries is that developed catalysts exhibit sluggish activity for both oxygen reduction and evolution reactions (ORR and

OER) or only remain active for one of the reactions (different ORR/OER rates).^[1–5] This can result in high overpotentials—excess energy above its thermodynamic value (2.96 V)—required to form and decompose lithium peroxide (Li₂O₂) at the cathode during discharge (ORR) and charge (OER) processes, respectively. Numerous metal catalysts such as platinum (Pt), gold (Au), and ruthenium (Ru), as well as non-metallic catalysts such as transition-metal oxides, transition-metal dichalcogenides, and carbon-based catalysts, have been employed to resolve this issue, however, no major breakthrough has been reported to date.^[4,6–11] Therefore, designing a highly active catalyst that can minimize the energy barriers—excess input energy—to form and decompose Li₂O₂ nanoparticles at the cathode is a key challenge for the development of this technology.

Electrocatalytic properties of transition metal phosphides have received great attention and been subject of theoretical and experimental studies.^[12–16] Wang et al. demonstrated a convenient and straightforward approach to the synthesis of a 3D self-supported Ni₅P₄Ni₂P nanosheet cathode, very stable in acidic medium with an outstanding hydrogen evolution reaction (HER) activity.^[17] Some other studies include development of

A. Kondori, M. Esmaeilirad, P. Navarro Munoz Delgado, S. Maghsoudipour, J. Hayes, Prof. M. Asadi
Department of Chemical and Biological Engineering
Illinois Institute of Technology
Chicago, IL 60616, USA
E-mail: m.asadi@iit.edu

Dr. Z. Jiang, Dr. A. Kakekhani, Prof. A. M. Rappe
Department of Chemistry
University of Pennsylvania
Philadelphia, PA 19104-6323, USA

The ORCID identification number(s) for the author(s) of this article can be found under <https://doi.org/10.1002/adma.202004028>.

DOI: 10.1002/adma.202004028

M. Tamadoni Saray, Prof. R. Shahbazian-Yassar
Department of Mechanical and Industrial Engineering
University of Illinois at Chicago
Chicago, IL 60607, USA
Dr. K. Kucuk, Prof. C. U. Segre
Department of Physics and CSRR
Illinois Institute of Technology
Chicago, IL 60616, USA
Dr. C. S. Johnson
Chemical Sciences and Engineering Division
Argonne National Laboratory
Lemont, IL 60439, USA

inexpensive and active nickel-based catalysts for HER stable in both acid and base,^[18,19] and selective CO₂ reduction reaction (toward C₃ and C₄ products).^[20]

Recently, we have demonstrated that trimolybdenum phosphide (Mo₃P) nanoparticles can be a promising catalyst candidate, owing to its unique structure; its surface provides a high density of molybdenum (Mo) active sites with special electronic properties, that is, low work function and high density of d-orbital electrons at Fermi energy, which can be promising for electrocatalysis.^[21] The important role of surface reconstructions in catalysis, which renders the surface region of the catalyst atomically and geometrically distinct relative to the bulk, has been pointed out.^[22,23] A special type of surface reconstructions that can happen in an oxygen-rich environment is the formation of ultrathin oxide overlayers.^[24–26] Beyond transition metal-based catalysis, such oxidized overlayers have also shown their importance in carbon-based catalysts.^[27,28] Here, we report that a kinetically stable reconstructed oxide overlayer on Mo₃P boosts its electrocatalytic performance toward exceptional ORR and OER activities, that is, current densities of 7.21 mA cm⁻² at 2.0 V versus Li/Li⁺ (ORR) and 6.85 mA cm⁻² at 4.2 V versus Li/Li⁺ (OER) in a non-aqueous electrolyte, exceeding the performance of existing catalysts reported to date.^[29–38] Using this catalyst, we also have demonstrated a Li-air battery cell with a long cycle life of 1200, low discharge and charge overpotentials of 80 and 270 mV, respectively, and high energy efficiency (90.2%) at the first cycle.

The Mo₃P nanoparticles were synthesized using a facile colloidal chemistry method followed by a thermal sintering process (Section S1, Supporting Information).^[21,39] X-ray diffraction (XRD) patterns of the studied catalyst are shown in Figure S1, Supporting Information confirming the crystalline structure of the synthesized catalysts (Section S2, Supporting Information) with an average crystallite size of 25 nm using the Scherrer equation (Section S2, Supporting Information). The preparation and characterization of other studied catalysts, such as, MoS₂ nanoflakes, Pt, and Au nanoparticles are explained in Sections S1 and S2, Supporting Information.

We evaluated the electrocatalytic performance of Mo₃P nanoparticles for ORR and OER in a non-aqueous electrolyte by performing cyclic voltammetry (CV) experiments in our custom-designed three-electrode electrochemical cell (Figure S2, Section S3.1., Supporting Information). The electrolyte was composed of 0.3 M Bis(trifluoromethane)sulfonimide (LiTFSI) lithium salt dissolved in a 75:25 volumetric ratio of dimethyl sulfoxide (DMSO) and 1-ethyl-3-methylimidazolium tetrafluoroborate (EMIM-BF₄) electrolyte saturated with pure oxygen (O₂). As shown in Figure S3a (Section S3.2., Supporting Information), the recorded ORR and OER activities for Mo₃P nanoparticles are 7.21 mA cm⁻² (at 2.0 V vs Li/Li⁺) and 6.85 mA cm⁻² (at 4.2 V vs Li/Li⁺), respectively. The results also indicate a negligible difference in observed ORR and OER current densities (about 5%) in the potential window of 2.0 to 4.2 V versus Li/Li⁺ for Mo₃P nanoparticles suggesting its high activity for both ORR and OER. Moreover, as shown in Figure S4, Supporting Information, the maximum OER activity (at 4.2 V vs Li/Li⁺) for Mo₃P nanoparticles is 3.6, 5.6, and 74 times higher than MoS₂ nanoflakes (1.88 mA cm⁻²), Pt (1.23 mA cm⁻²), and Au nanoparticles (0.93 mA cm⁻²), respectively. Similarly, the

maximum ORR activity (at 2.0 V vs Li/Li⁺) for Mo₃P is 1.9, 2.7, and 3.2 times higher than MoS₂ nanoflakes (3.84 mA cm⁻²), Pt (2.71 mA cm⁻²), and Au nanoparticles (2.23 mA cm⁻²), respectively, under the identical electrochemical conditions offering superior ORR/OER electrocatalytic activities of Mo₃P nanoparticles compared to the studied catalysts (Section S3.2., Supporting Information). Moreover, Mo₃P nanoparticles exhibit higher activities for ORR/OER comparing with the state-of-the-art catalysts yet reported as shown in Figure S5 (Section S3.2., Supporting Information).^[29–38]

The actual catalytic activity of Mo₃P nanoparticles was evaluated by calculating the turnover frequency for ORR (TOF_{ORR}) and OER (TOF_{OER}) and comparing it with the studied catalysts under identical electrochemical conditions (Section S3.3., Supporting Information). The results shown in Figures S5a,b, Supporting Information indicate higher TOF_{ORR} and TOF_{OER} for Mo₃P nanoparticles over entire range of overpotentials compared to MoS₂ nanoflakes, Au and Pt nanoparticles (Section S3.3., Supporting Information) confirming superior catalytic activity of this catalyst for both reactions.

We performed a kinetic study by drawing Tafel plots for ORR and OER to characterize the intrinsic catalytic behavior of Mo₃P nanoparticles compared with the best reported catalysts in non-aqueous media (Figure 1). Tafel plots for ORR (Figure 1a) and OER (Figure 1b) were obtained from iR-corrected CV experiments (Section S3.4., Supporting Information). As shown in Figure 1a, Mo₃P nanoparticles exhibits a Tafel slope of 35 mV dec⁻¹ and a remarkably low onset potential of 4.0 mV (with respect to the Li₂O₂ formation standard potential at 2.96 V vs Li/Li⁺). However, as shown in Figure 1a, MoS₂ nanoflakes, Pt and Au nanoparticles show slightly higher Tafel slopes (41, 39, and 46 mV dec⁻¹, respectively). Moreover, the Tafel plot study for OER indicate Mo₃P nanoparticles have a Tafel slope of 38 mV where Tafel slopes of 72, 136, and 132 mV dec⁻¹ were obtained for MoS₂ nanoflakes, Pt, and Au nanoparticles, respectively (Figure 1b). The Mo₃P nanoparticles also show an onset potential of 5.1 mV for OER (Figure 1b). These results suggest a lower charge transfer resistance and a higher intrinsic catalytic activity for Mo₃P nanoparticles compared to other catalysts.^[29–38]

Benefiting from exceptional ORR/OER performance of Mo₃P nanoparticles, we tested the performance of this catalyst as the cathode in a Li-air battery cell that works in an air-like atmosphere composed of 78% nitrogen (N₂), 21% O₂, water (H₂O, relative humidity (RH) of about 45%), and 500 ppm carbon dioxide (CO₂). A 0.3 M LiTFSI dissolved in a 72:25 volumetric ratio of DMSO:EMIM-BF₄ mixture with 25 × 10⁻³ M of each of 2,2,6,6-tetramethyl-1-piperidinyloxy (TEMPO) and 2,5-di-tert-butyl-1,4-benzoquinone (DBBQ) redox mediators (RMs) was used as the electrolyte (Section S4, Supporting Information).

The binder-free cathode was prepared by direct synthesis of Mo₃P nanoparticles on a carbon substrate (with a mass ratio of 1:2) by a colloidal chemistry technique and used as the cathode in our custom designed Li-air battery cell (Sections S1 and S4, Supporting Information). Figure 2a shows the discharge and charge profiles of the Li-air battery system working up to 500 mAh g_{cath}⁻¹ specific capacity—measured based on the total mass of the cathode—at 1 C rate (a current density of 500 mA g_{cath}⁻¹). As shown in Figure 2a, the first discharge process reaches 2.88 V versus Li/Li⁺ after 1 h, replicating a

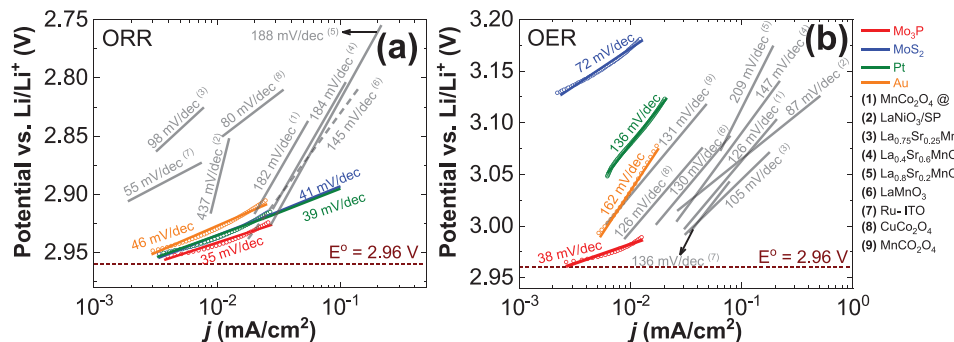


Figure 1. Mechanistic study—Tafel plots—for evaluating the ORR/OER kinetics of catalysts in non-aqueous media. A comparative study of the reported catalysts in the literature and our synthesized Mo₃P nanoparticles. a,b) Tafel plots for ORR (a) and OER (b) are obtained from *iR*-corrected cyclic voltammetry (CV) experiments (Section S3, Supporting Information) and CV results for the reported catalysts in the literature.^[29–38]

capacity of 500 mAh g_{catald}⁻¹. During the first charge process, the potential of the cell increases to 3.23 V versus Li/Li⁺, yielding a capacity of 500 mAh g_{catald}⁻¹. Considering the reversible thermodynamic formation potential of Li₂O₂ (2.96 V vs Li/Li⁺), these results indicate discharge and charge overpotentials of about 80 and 270 mV, respectively, at the first cycle, offering a remarkable performance for the developed Li-air battery system.

The cyclability of the system was then evaluated by performing charging and discharging experiments at 1 C rate and constant specific capacity of 500 mAh g_{catald}⁻¹ with respect to the number of cycles. The cycling results shown in Figure 2a indicate that this system can work up to 1200 continuous cycles in a cut-off potential gap of 2.4 V (2.2–4.6 V vs Li/Li⁺), exceeding the state-of-the-art Li-air and Li–O₂ batteries (Figure S9, Section S4, Supporting Information).^[29–38]

We also studied the variations in the charge and discharge potentials with respect to the number of cycles (Figure 2b). As shown in Figure 2b, three different regions are observed in the charge profile of our Li-air battery cell, (i) from cycle 1 to 100 where there is a sharp increase in the charge potential from 3.23 V versus Li/Li⁺ to 3.81 V versus Li/Li⁺ (\approx +6 mV per cycle), (ii) from cycle 101 to 1000 where the charge potential gradually increases from 3.82 V versus Li/Li⁺ to 4.34 V versus Li/Li⁺ (\approx +0.5 mV per cycle), and (iii) from cycle 1001 to 1200 with a potential variation from 4.34 V versus Li/Li⁺ to 4.64 V versus Li/Li⁺ (\approx +1.5 mV per cycle). However, we observed a slight

variation in the discharge potential (0.26 V) during the first 1000 cycles (2.88–2.62 V vs Li/Li⁺) where it sharply drops after 1000 cycles to reach 2.22 V versus Li/Li⁺ at the 1200th cycle.

Next, we studied the columbic efficiency (C.E.), energy efficiency, and the observed potential gap over 1200 cycles at 1 C rate (Figure 2c). As shown in this figure, the developed Li–air cell exhibits a very stable cyclability while retaining nearly 100% C.E. over 1200 cycles of galvanostatic cycling at 1 C discharge/charge rates (green dots in Figure 2c). The potential gap shown in this figure (blue dots in Figure 2c) consists of three different regions, similar to that observed in charge potentials in Figure 2b, (i) from cycle 1 to 100 where the potential gap increases from 0.35 V at the 1st cycle to 0.98 V at the 100th cycle, (ii) from cycle 101 to 1000 with a gradual increase from 0.97 to 1.84 V, (iii) from cycle 1001 to 1200 from 1.84 to 2.42 V. As shown in Figure 2c, the energy efficiency of the first cycle is 90.2% and it gradually drops to 65.4% after 1000 cycles. The efficiency of the cell further decreases to 55.4% at the 1200th cycle. Moreover, the Mo₃P catalyst shows deep charge and discharge capability of 192 h as indicated in Figure S10 (Section S5, Supporting Information).

To gain more insight into the effect of TEMPO and DBBQ RMs on the performance of our Li–air battery cell, we performed a set of control experiments by cycling two identical Li–air battery cells with and without the RMs (Section S6, Supporting Information). The results shown in Figure S11, Supporting

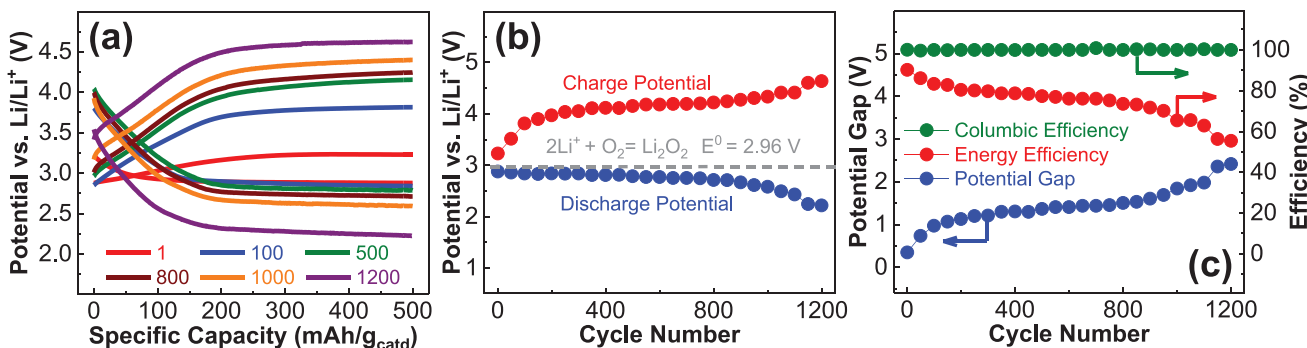


Figure 2. The Li–air battery performance using Mo₃P cathode. a) Charge/discharge profiles over 1200 cycles at a constant density of 500 mA g_{catald}⁻¹, and a constant specific capacity of 500 mAh g_{catald}⁻¹. The electrolyte is 0.3 M LiTFSI dissolved in DMSO:EMIM-BF₄ (75/25 v/v%) with 25 × 10⁻³ M of each TEMPO and DBBQ RMs. b) Discharge and charge potential values over 1200 cycles. The graph shows the stable discharge overpotential with an average value of 2.77 V over 1000 cycles. c) Changes in columbic efficiency, energy efficiency, and potential gap over 1200 cycles.

Information indicate that TEMPO and DBBQ RMs in the battery electrolyte work remarkably well with Mo₃P nanoparticles to further decrease discharge and charge overpotentials (≈ 30 and ≈ 90 mV, respectively at the 150th cycle). This is in agreement with previous studies that suggest the addition of RMs acts as mobile charge carriers in the liquid electrolyte to promote the solvent-based growth mechanism resulting in reducing charge and discharge overpotentials in Li-air battery cells.^[40–45]

In order to study the physical properties of the discharge products, scanning electron microscopy (SEM), Raman spectroscopy, XRD, and X-ray photoelectron spectroscopy (XPS) experiments were used to characterize the surface of the charged/discharged cathodes at different cycles (Sections S7–S10, Supporting Information).

The SEM images of the charged/discharged cathodes at different cycles, such as, 1, 50, and 200, are shown in Figure 3a–f. The results indicate agglomeration of products that were epitaxially grown on the cathode surface during the discharge process suggesting the solvent-based growth mechanism for our developed Li-air battery cell.^[46–49] The SEM images of the cathodes also show that the formed products were completely

disappeared after the charge process (Section S7, Supporting Information). The SEM images of higher cycle numbers, such as, 800, 1000, and 1200, are shown in Figures S12–S13, Section S7, Supporting Information.

Next, we carried out *in situ* differential electrochemical mass spectroscopy (DEMS) to determine the number of electrons transferred per O₂ during the discharge and charge processes (Section S8, Supporting Information). The DEMS experiments of the first discharge and charge processes were performed in 5 C rate (2500 mA g_{catalyst}⁻¹ current density) to a specific capacity of 500 mAh g_{catalyst}⁻¹ (Figure 3g,h). Figure 3g shows the *in situ* DEMS result of the discharge process, presenting a rapid decrease of the O₂ signal upon discharge with calculated electron to O₂ ratio (e⁻/O₂) of 2.05, while no change was observed in the CO₂ and H₂O signals. The results for the charge process (Figure 3h) indicate the rise of O₂ signal while CO₂ and H₂O signals remained unchanged confirming the evolution of O₂ gas due to decomposition of Li₂O₂. As shown in Figure 3h, the results also indicate e⁻/O₂ of 2.02 confirming reversible decomposition of Li₂O₂ in our Li-air battery cell (Section S8, Supporting Information).

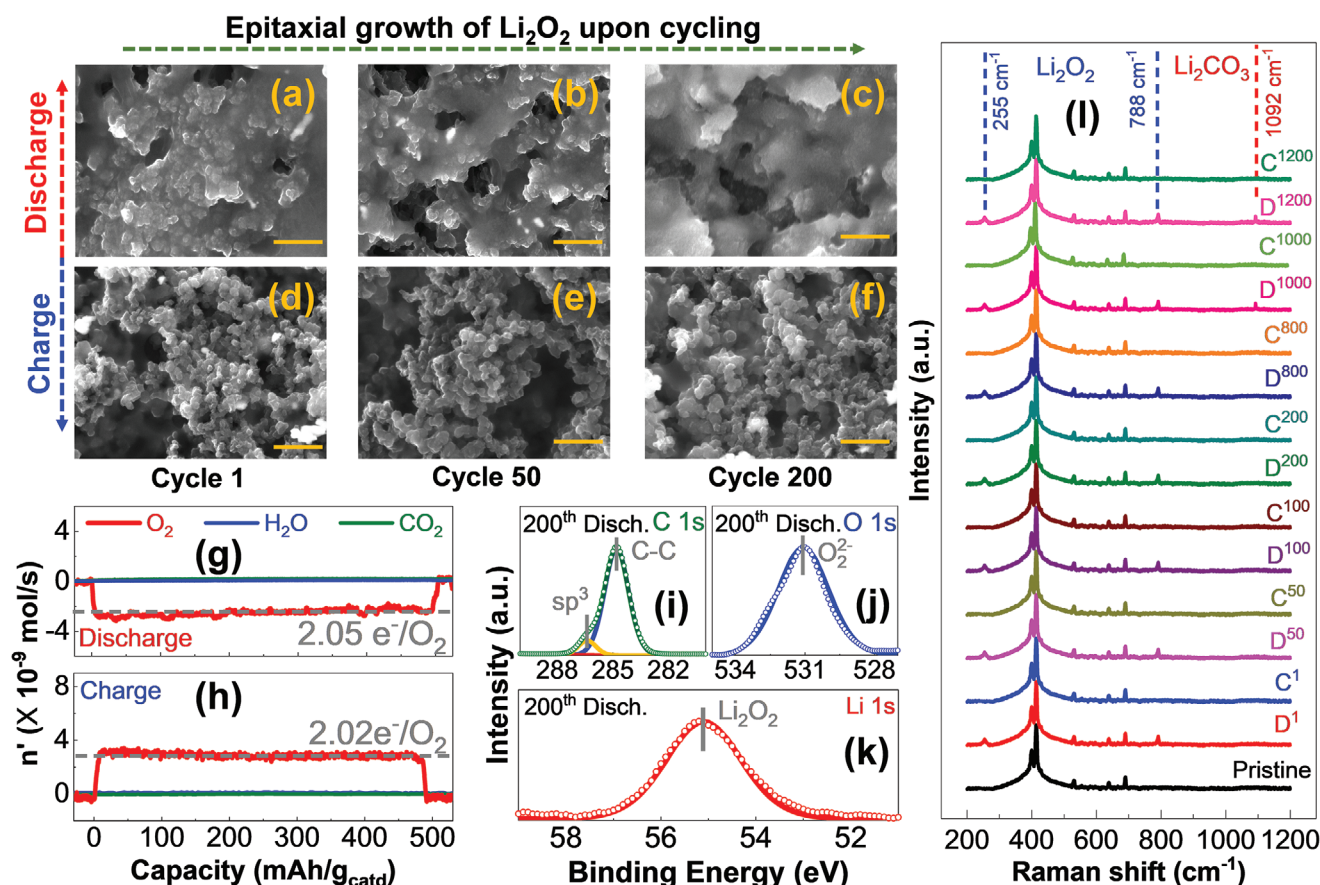


Figure 3. Discharge and charge characterization of Mo₃P cathode in the Li-air battery. a–f) Scanning electron microscopy (SEM) image of the cathode after the charge and discharge process after 1, 50, and 200 cycles. g) In situ differential electrochemical mass spectroscopy (DEMS) of the discharge and h) charge processes with constant current density of 2500 mA g_{catalyst}⁻¹. Calculated molar quantiles of evolved O₂ over the charge cycle confirming two electron transfer reaction corresponding to the lithium peroxide (Li₂O₂) formation/decomposition. i–k) C 1s, O 1s and Li 1s X-ray photoelectron spectra (XPS) of discharged battery after 200 cycles indicating peaks at 55.1 (Li 1s), 531.15 (O 1s) eV suggesting the formation of the Li₂O₂ nanoparticles l) Raman spectra of charged and discharged cathodes of 1, 50, 100, 200, 800, 1000, and 1200 cycles. Peaks observed at 255 and 788 cm⁻¹ correspond to Li₂O₂ formation whereas the peak at 1092 cm⁻¹ corresponds to Li₂CO₃ formation.

Furthermore, we performed XPS experiment for the discharged cathodes at different cycles, such as, 1, 50, 100, 200, 800, 1000, and 1200, to precisely detect lithium-based species on the cathode surface (Section S9, Supporting Information). As shown in Figure 3i–k and Figure S15, Supporting Information, the O 1s and Li 1s spectra show distinguishable peaks at 531.1 and 51.1 eV, respectively, suggesting the formation of Li_2O_2 nanoparticles as the discharged product in all discharged samples up to 1000 cycles.^[50] The XPS results for 1000th cycle also reveal new peaks at 289.9, 55.6, and 531.9 eV in the C 1s, Li 1s, and O 1s spectra, respectively, in addition to the Li_2O_2 nanoparticles, suggesting the formation of Li_2CO_3 at the cathode surface after 1000 cycles (Figure S16, Section S9, Supporting Information).

Figure 3l shows the Raman spectra of the charged and discharged cathodes at different cycles, such as, 1, 50, 100, 200, 800, 1000, and 1200, comparing with the pristine cathode (Section S9, Supporting Information). As shown in this figure, we observed two distinguishable peaks at 255 and 788 cm^{-1} which correspond to the formation of Li_2O_2 nanoparticles during discharge processes up to 1000 cycles as the discharge product in our Li-air battery cell. It is worth mentioning that the Raman spectra for all discharged cathodes up to 1000 cycles do not show peaks corresponding to other lithium-based species such as Li_2CO_3 , LiOH , or LiO_2 . Moreover, Raman spectra of the cathodes indicate that the Li_2O_2 peaks, at 255 and 788 cm^{-1} , were disappeared after the charge process suggesting reversible formation and decomposition Li_2O_2 nanoparticles in our Li-air battery cell.^[50,51] However, the results for the charge and discharge of 1000 and 1200 cycles confirm the presence of a new peak at 1092 cm^{-1} in addition to the Li_2O_2 peaks that is correlated to the formation of Li_2CO_3 as a side product (Section S10, Supporting Information).^[52,53]

To further confirm the presence of the Li_2O_2 nanoparticles, we also performed XRD experiments for the charged and discharged cathodes at different cycles, such as, 1, 50, 100, 200, 800, 1000, and 1200, and compared them with the pristine cathode (Section S11, Supporting Information). The XRD patterns of the all discharged cathodes indicate peaks at 32.3°, 34.4°, 48.0°, and 48.7° corresponding to the (100), (101), (004), and (103) crystal planes of Li_2O_2 nanoparticles (Figure S18, Section S10, Supporting Information) that have completely disappeared after the charge in all cycles confirming the reversible formation and decomposition of the Li_2O_2 nanoparticles.^[50,51] Moreover, as shown in Figures S18–S19, Supporting Information, new peaks appear at 21.85°, 29.95°, and 30.50° corresponding to the (110), (111), and (200) crystal planes of Li_2CO_3 nanoparticles, revealing the formation of Li_2CO_3 nanoparticles as a side product during the discharge processes of 1000 to 1200 cycles.^[52,53] However, there is no Li_2CO_3 peak in the XRD patterns after the charge of 1000 and 1200 cycles, suggesting that the Li_2CO_3 nanoparticles were decomposed after the charge (Section S10, Supporting Information).

To identify the origin of Li_2CO_3 formation in our developed Li-air battery cell, we studied the stability of the cathode, anode, and electrolyte at different cycles. At first, the stability of the Mo_3P cathode was studied by performing atomic scale characterization using scanning transmission electron microscopy (TEM), high resolution TEM (HR-TEM) and electron

energy loss spectroscopy (EELS) after the first discharge process (Section S12, Supporting Information). HR-TEM images of the Mo_3P nanoparticles after the first discharge process are shown in Figure 4a,b, suggesting a well-remained crystal structure in [001] zone axis with the corresponding Fast Fourier transform (FFT) in the inset of Figure 4a as well as a tetragonal crystal system of $\bar{I}\bar{4}2\text{m}$ space group of Mo_3P . As shown in Figure 4a,b, a boundary can be observed at the surface of Mo_3P nanoparticles, suggesting the presence of a different structure of Mo atoms. To find out more about such a difference in the structure of Mo_3P nanoparticles at the surface, we measured intensity line profiles (Figure 4c) of the region indicated in the dashed box in Figure 4b. As shown in Figure 4c, a transition was observed in the lattice spacing $d_{310} = 3.12 \text{ \AA}$ in the bulk to $d_{220} = 1.44 \text{ \AA}$ at the surface which corresponds to the rock-salt face centered cubic crystal structure of MoO with lattice constant $a = 4.08 \text{ \AA}$.^[54] This change in the lattice spacing and our EELS mapping results (Section S12, Supporting Information) confirm the presence of a MoO overlayer with a thickness of about 2 to 3 nm.

To further study the stability of the Mo_3P cathode and the MoO overlayer during the repeated cycles, we performed XPS experiments for the discharged cathodes at different cycles, such as, 1, 200, and 1200 and compared them with the pristine sample (Figure 4d; Figure S17, Section S9, Supporting Information). As shown in Figure 4d, peaks at 232.7 and 229.5 eV indicate the presence of standard $\text{Mo } 3\text{d}_{3/2}$ and $3\text{d}_{5/2}$ peaks, corresponding to the Mo^{3+} oxidation state whereas the peaks at 231.9 and 228.7 eV show the presence of standard $\text{Mo } 3\text{d}_{3/2}$ and $3\text{d}_{5/2}$ peaks that are attributed to the Mo^{4+} oxidation state in Mo_3P nanoparticles.^[21] Moreover, our XPS results for the discharged cathode at the first cycle show the broadening of the observed peaks compared to the pristine sample, suggesting the formation of MoO (Mo^{2+}) with standard $3\text{d}_{3/2}$ and $3\text{d}_{5/2}$ peaks at 231.0 and 228.1 eV, respectively.^[55,56] The XPS analyses of the discharged cathode samples after different cycles, such as, 1st, 200th, and 1200th confirm Mo_3P nanoparticles and MoO overlayer remain stable over 1200 cycles (Figure 4d). These results are further confirmed by comparing the XRD and Raman spectroscopy results for the cathode samples over cycling with the pristine sample (Sections S10 and S11, Supporting Information).

Next, we studied the stability of the anode by performing XPS experiments for the Li anode after the discharge processes of different cycles, such as, 10, 50, 200, 800, 1000, and 1200 comparing with the pristine Li anode (Figure S22, Section S13, Supporting Information). Our results indicate the formation of the Li_2CO_3 layer that is stable over 1200 cycles. Moreover, we did not observe any other peaks at the anode surface, suggesting that the Li_2CO_3 layer effectively protects the Li anode from degradation in presence of the air components such as nitrogen (N_2), O_2 , and H_2O , consistent with our previously reported studies (Section S13, Supporting Information).^[50]

Furthermore, we investigated the stability of the electrolyte using ^1H and ^{13}C nuclear magnetic resonance (NMR) spectroscopy experiments for electrolyte samples after discharge processes of different cycles, such as, 10, 100, 200, 800, 1000, and 1200, and compared them with the fresh electrolyte (Figure 4e; Figures S23–S26, Section S14, Supporting Information). Our

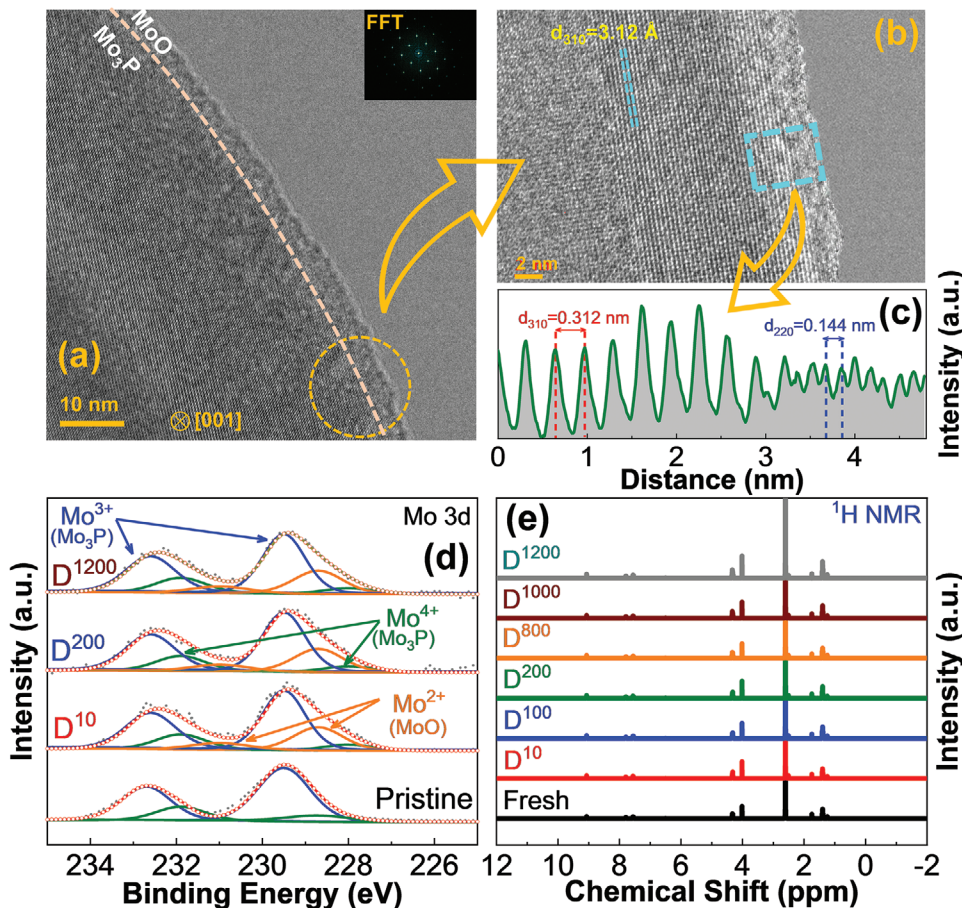


Figure 4. Evaluating the stability of the Mo₃P cathode in the Li-air battery. a) High-resolution transmission electron microscopy (HR-TEM) image of Mo₃P nanoparticles at [001] zone axis (scale bar, 10 nm). The inset in (a) shows the corresponding fast Fourier transform (FFT). b) HR-TEM image of the selected area shown by the dashed circle in (a) (scale bar: 2 nm). c) Corresponding intensity line profile of the selected area shown by the dashed rectangle in (b). d) Mo 3d X-ray photoelectron spectra (XPS) for the cathode samples after discharge processes of different cycles, that is, 10, 200, and 1200, compared to the pristine sample. e) ¹H NMR spectroscopy of the electrolyte after discharge processes over 1200 cycles compared to the fresh electrolyte.

¹H NMR analyses of the fresh electrolyte with cycled samples (Figure 4e) show a trace amount of H₂O (peak at 2.56 ppm in ¹H NMR) in the electrolyte that is due to the RH of 45%. However, our ¹H and ¹³C NMR results do not indicate any change in the position and intensity of the peaks corresponding to H₂O and DMSO compounds up to 1200 cycles confirming that the H₂O molecules do not react with DMSO (Figure 4e; Figures S23 and S25, Section S14, Supporting Information). This is also consistent with our characterization results where no LiOH peak was observed on the cathode.

Our NMR results (Figure 4e; Figures S23–S26, Supporting Information) also indicate that peaks corresponding to the presence of TEMPO in the electrolyte have disappeared after 1000 cycles, suggesting the deactivation of TEMPO, which results in rising charge potentials as observed after this cycle (Figure 2b). This change in the charge potentials increases possible reactions of cathode carbon materials in the presence of oxygen species leading to formation of Li₂CO₃ nanoparticles as observed in our Raman spectroscopy, XRD, and XPS results of the cathode at cycles 1000 to 1200 (Section S9–S11, Supporting Information).^[57–59]

However, the observed sharp increase of charge potentials in the first 100 cycles (Figure 2b) might be correlated to the saturation of electrolyte with discharge product (Li₂O₂ and LiO₂) that affects mass transports and the ionic diffusion properties of the electrolyte as we did not observe any degradation of the cell components, such as, cathode, anode and the electrolyte over 1000 cycles.^[60–64]

Ultimately, in order to better understand mechanisms leading to the favorable ORR and OER performance of the catalyst, we performed a systematic first-principles study of discharge and charge reactions on Mo-terminated Mo₃P (110) (Section S15, Supporting Information). The Mo₃P (110) slab with pure Mo termination was employed because our calculation indicates this structure is more thermodynamically stable than MoP_{0.5} terminated surfaces in the O₂ environment (Figure S27a, Section S15, Supporting Information), and a low-index (110) facet can be a good model for the majority surface sites of experimentally relevant Mo₃P nanoparticles. Such facet has also been employed successfully to model the high HER activity of Mo₃P nanoparticles with low overpotentials.^[21,65] At first, we determined the surface reconstruction of the Mo₃P (110) slab under

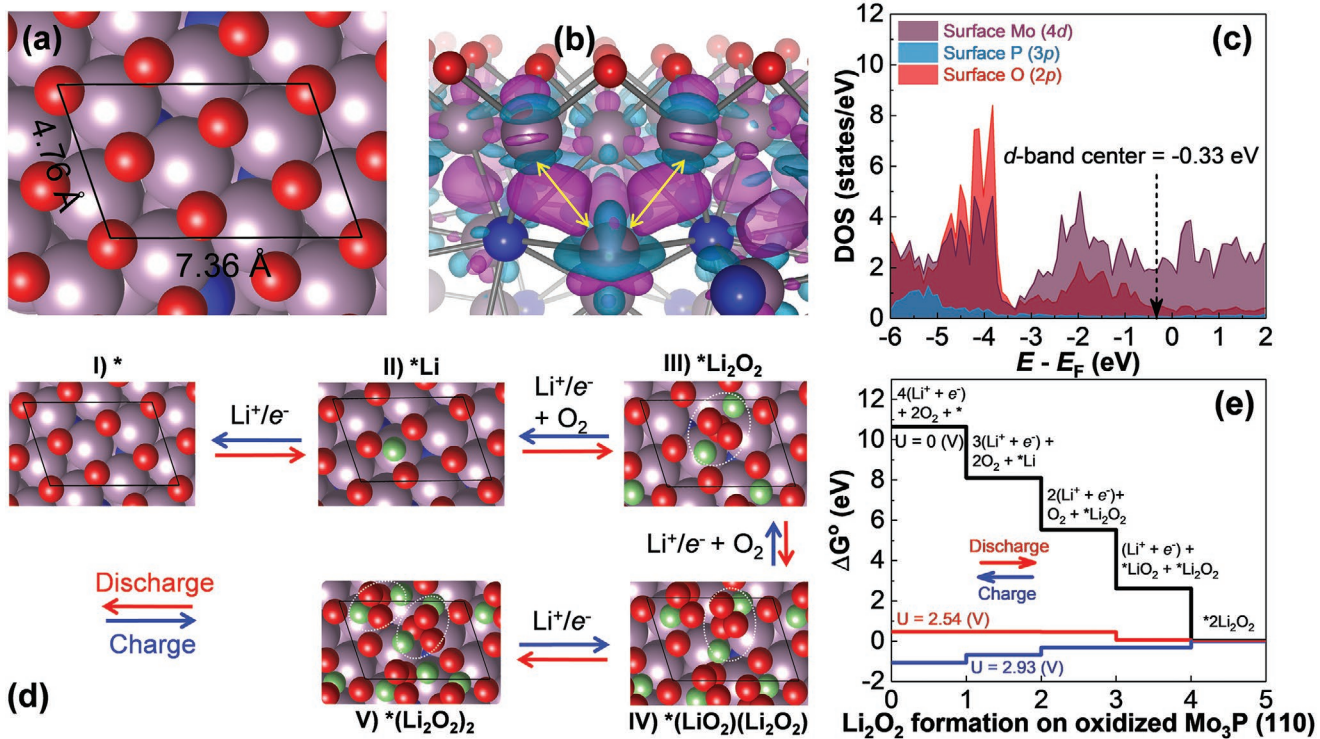


Figure 5. Computational study of the Li-air battery—charge and discharge mechanisms a) Top view of oxidized Mo_3P (110) surface ($a = 4.76 \text{ \AA}$, and $b = 7.36 \text{ \AA}$ are the in-plane lattice constants), where the light purple, blue, and red balls are Mo, P, and O atoms, and where the surface repeat unit is highlighted by the parallelogram. b) Electron density difference map of the chemisorption between the MoO layer and the substrate, where the magenta and cyan colors indicate regions of space with increased and decreased electron density, respectively. c) Projected density of states (PDOS) for Mo_3P (110) in oxidized form. The d-band center of Mo atoms on the surface is also shown. d) The most thermodynamically favorable mechanisms of ORR (discharge) and OER (charge) processes on oxidized Mo_3P (110) slab. Each Li_2O_2 is shown with a white dashed oval. e) Calculated free energy diagram for the discharge (ORR from right to left) and charge (OER from left to right) reactions on the oxidized Mo_3P (110). $U = 2.54$ and 2.93 V are the highest and lowest potentials where discharge and charge are still downhill in all steps of Mo_3P (110), respectively.

the operating conditions (oxygen-rich environment). We find that this surface is highly active toward O_2 molecules leading to spontaneous dissociative adsorption and creation of a surface oxide layer. This layer consists of O atoms adsorbed on the hollow sites of Mo-terminated Mo_3P (110) (Figure 5a). Due to the O_2 -rich environment in which Li-air batteries are operated, the high O coverage surface is favored. We also found that the surface is saturated by O_2 in a ratio of Mo: O = 1: 1, with an average adsorption energy of -3.0 eV per O atom. Bader charge analysis of pristine Mo_3P (110) surfaces shows that the surface Mo atoms are electron rich ($\approx +0.1$) compared to the sub-surface Mo (bulk Mo atoms) (in the range of $+0.5$ to $+1.0$) due to the lower coordination of surface Mo by P atoms. Furthermore, the surface Mo atoms are nearly neutral meaning that the surface Mo layer is metallic with high adsorption affinity for electronegative O atoms. This is in agreement with Figure S27d, Supporting Information indicating metallic surface Mo 4d-electrons, which do not have significant hybridization with P 3p-electrons (Section S15, Supporting Information). As a result, a surface MoO monolayer will be formed, which serves as the active catalytic substrate for ORR and OER, that is also observed in our XPS, XRD, and STEM characterization experiments (Figure 4a–d; Figures S17 and S18, Sections S9 and S11, Supporting Information).^[66,67] To further confirm the existence of oxide layer, we have performed ultraviolet photoelectron

spectroscopy (UPS) experiments of the cathode after the first charging process (Section S16, Supporting Information). Our measurements (Figure S29, Supporting Information) indicate 0.25 eV lower work function for the oxidized Mo_3P (3.18 eV) compared with pristine Mo_3P (3.43 eV) further supporting the existence of the oxide overlayer on Mo_3P that can be a reason for high activity of this catalyst for both ORR and OER.^[39,68–73]

In addition, we studied the stability of this MoO monolayer by computing its further oxidation to form MoO_3 , which is the most earth-abundant Mo oxide. Our density functional theory (DFT) results show that although Mo_3P is not thermodynamically stable (e.g., relative to MoO_3 and P_2O_5) in an O_2 -rich environment in agreement with experimental observations,^[74] the MoO monolayer can enhance the kinetic stability of Mo_3P (Section S15, Supporting Information). This is in agreement with our characterization results, such as, XPS, XRD, Raman spectroscopy, SEM, and STEM, where we found Mo_3P cathode to be stable over 1200 cycles.

Equipped with the knowledge of the surface reconstruction and composition, we simulated different ORR and OER steps on Mo_3P (110). In order to compare the thermodynamics of different mechanisms, we studied two different pathways to form adsorbed Li_2O_2 units: with 1) a $\cdot\text{LiO}_2$ intermediate, that is, O_2 adsorption concurrent with the first Li^+ adsorption, and 2) a $\cdot\text{Li}$ intermediate, that is, O_2 adsorption concerted with the second

Li^+ adsorption (Section S18, Supporting Information).^[49,75,76] We found that the latter (${}^*\text{Li}$ intermediate) is more favorable for adsorption of the first Li_2O_2 unit, while the former (${}^*\text{LiO}_2$ intermediate) is the preferred mechanism for a subsequent adjacent Li_2O_2 unit. Figure 5d shows the most thermodynamically favorable pathway to produce two Li_2O_2 units on the oxidized Mo_3P (110) slab during the discharging reaction (ORR), with detailed ΔG in Table S4 (Section S18, Supporting Information).

We also found that for the initial Li^+ adsorption ($\Delta G = -2.54 \text{ eV}$ at $U = 0 \text{ V}$) process Li^+ prefers the O_3 hollow sites rather than bridge or top sites due to the formation of three ionic-covalent bonds between Li and O (Figure S27b, Section S15, Supporting Information). It is also notable that not all O_3 hollow sites are favorable for the first Li^+ adsorption due to different electrostatics (Figure S27c, Section S15, Supporting Information). The first adsorbed Li^+ prefers an O_3 hollow site below which there is a P-coordinated Mo. The P-coordination from below shifts Mo (with a partially positive charge) downward, reducing repulsion and rendering the electrostatic potential well deeper for Li^+ adsorption. The charging reaction (OER) follows the same reaction steps in the opposite direction (blue lines) as shown in Figure 5d.

Next, we calculated the free-energy diagrams at different applied potentials (U), where the effect of voltage (potential) is included by introducing a $-n\text{eU}$ term to the ΔG expression for electrochemical steps involving a number (n) of Li^+/e^- transfer reactions (Figure 5e).^[77,78] The ideal equilibrium potential (U_0) for Li_2O_2 formation is 2.60 V in our calculations (Section S15, Supporting Information), which is very close to the value of 2.62 V previously reported.^[49] The overpotential (η) is identified by $\eta_{\text{discharge}} = U_0 - U_{\text{discharge}}$ or $\eta_{\text{charge}} = U_{\text{charge}} - U_0$, where $U_{\text{discharge}}$ and U_{charge} refer to the maximum and minimum applied potential that guarantees that all electrochemical steps are energetically favorable in the discharge and charge processes, respectively. As seen in Figure 5e, we found the $\eta_{\text{discharge}} = 0.06 \text{ V}$ and $\eta_{\text{charge}} = 0.33 \text{ V}$ on the oxidized Mo_3P (110) surface, which is very close to our experimental measurements ($\eta_{\text{discharge}} = 0.08 \text{ V}$ and $\eta_{\text{charge}} = 0.27 \text{ V}$). We also found that the potential determining step (PDS) during discharge is the initial Li^+/e^- transfer (configuration I to II in Figure 5d), while the release of ${}^*\text{LiO}_2$ (configuration IV to III in Figure 5d) is the PDS for the charging reaction. During discharge, the catalytic Li_2O_2 production takes place on the MoO monolayer (oxidized top layer of Mo_3P) with a DFT-derived overpotential of 0.06 V. The Li_2O_2 units can then transfer (via ionic liquid) to agglomerated Li_2O_2 particles, also confirmed by SEM image shown in Figure 3a–f, (Section 19, Supporting Information), leaving a clean MoO layer behind for further catalysis of the Li_2O_2 production.^[79,80,63] Our DFT-derived and experimental discharge overpotentials on Mo_3P are smaller than the values calculated on the bulk Li_2O_2 surface (0.33 V on the thermodynamically stable majority facet (0001) and 0.12 V on kink sites),^[49] confirming the viewpoint that discharge takes place via catalytic MoO monolayer. For the charging process on the other hand, there can be two possible contributions: 1) dissolution of Li_2O_2 from the MoO monolayer, 2) dissolution of Li_2O_2 from the surface of the agglomerated Li_2O_2 particles formed during the discharge. As mentioned above, the overpotential for the former is 0.33 V. Regarding the latter process, the overpotential

for the decomposition of Li_2O_2 from its thermodynamic stable facet, (0001), (1100), etc.^[49,81,48] is calculated in the literature to be 0.36 V, while at surface defect sites, for example, kinks it can be as low as 0.19 V, two values that sandwich our experimentally measured 0.27 V charge overpotential.^[49] Thus, we conjecture that at the beginning of the charging the Li_2O_2 dissolution happens from agglomerated particles (most probably through defect sites, e.g., kinks), while toward the end (where most of the agglomerated Li_2O_2 is dissolved) the dissolution from the Mo_3P catalyst becomes more important. Nevertheless, since the overpotentials for these limiting cases are close, experimentally an overpotential of about 0.27 V will be measured throughout the charging.

The oxide monolayer can provide appropriate electrostatics for Li^+ adsorption (Figure S27c, Section S15, Supporting Information) in the O_3 hollow sites (forming from a quasi-hexagonal adsorbed O network), while still possessing mobile electrons at the Fermi level (due to its metallicity), which can trigger electrochemical charge transfer to form three Mo–O bonds (Figure S27b, Section S15, Supporting Information). Such a monolayer, MoO, has enough kinetic stability due to strong covalent and charge transfer interactions with the molybdenum phosphide layer beneath, as depicted in Figure 5b, making it possible for this monolayer to retain its epitaxial form during the course of the discharge. Additionally, the interaction of the deposited Li_2O_2 units with the surface is still in a range that, with the help of the ionic liquid solvent, can dissolve into the solvent,^[63,82–84] with only finite points of contact with the Mo_3P substrate, allowing the (oxidized) Mo_3P surface to continue catalyzing the Li_2O_2 production reaction as also observed in our SEM images shown in Figure 3a–f.

In summary, we have tested the catalytic performance of Mo_3P nanoparticles for ORR and OER in a non-aqueous medium and compared its reaction kinetics with the state-of-the-art catalysts in non-aqueous electrolytes. Our three-electrode electrochemical experimental results indicated that Mo_3P nanoparticles possess nearly the same catalytic activities for ORR (7.21 mA cm^{-2} at 2.0 V) and OER (6.85 mA cm^{-2} at 4.2 V). Our Tafel plot analyses suggest a faster charge transfer kinetics and high intrinsic catalytic activity of this catalyst for both ORR and OER (Tafel slopes of 35 and 38 mV dec⁻¹ for ORR and OER), outperforming the existing catalysts studied to date. Benefiting from the exceptional ORR/OER performance of Mo_3P nanoparticles, we also demonstrated a Li–air battery cell that works up to 1200 cycles at room temperature with an energy efficiency of 90.2% for the first cycle and an average C.E. of $\approx 100\%$. Characterization results such as XRD, XPS, Raman spectroscopy, and *in situ* DEMS indicated fully reversible formation and decomposition of Li_2O_2 as the discharge product up to 1000 cycles. Moreover, we found out that formation of a stable Li_2CO_3 layer protects the anode from side-reactions in contact with the air components as well as the electrolyte components. Our characterization results of the cell components, such as, cathode, anode, and electrolyte at different cycles suggest the deactivation of TEMPO which dramatically results in rising charge potentials, and thus, leading to the formation of Li_2CO_3 as a side-product, is the main reason for the performance loss after 1000 cycles. The DFT calculations point to formation of

a kinetically stable MoO monolayer on the Mo-terminated Mo₃P (110) surface sites leading to enhanced activities toward ORR and OER. The presence of such MoO layer was confirmed by a variety of characterization techniques, such as, XRD, XPS, UPS, STEM, and EELS mapping for the cathode samples after charge and discharge processes over 1200 cycles. Moreover, our computational results revealed that the low discharge overpotential can be attributed to the high activity of the MoO layer toward Li⁺/e⁻ transfer (the potential-determining step). The produced Li₂O₂ units transfer via the ionic liquid to agglomerated nanoparticles, leaving a clean MoO surface behind for further catalysis. Additionally, the results indicated that the observed low charge overpotential is due to the combination in dissolution of Li₂O₂ units from defect sites at early charge stages and its later dissolution through Mo₃P where the release of *LiO₂ intermediate is the PDS. The developed surface reconstructed Mo₃P catalyst with kinetically stable oxidized overlayer offers significant promise in the advancement of sustainable energy storage systems, owing to its unique electronic and structural properties discovered in our Li-air battery cell.

Supporting Information

Supporting Information is available from the Wiley Online Library or from the author.

Acknowledgements

M.A. work was supported by Illinois Institute of Technology start-up funding, Wanger Institute for Sustainable Energy Research (WISER) seed fund (262029 221E 2300), and the Soft and Hybrid Nanotechnology Experimental (SHyNE) Resource (NSF ECCS-1542205) funding. The authors acknowledge use of the Keck-II facility of Northwestern University's NUANCE Center, which has received support from the SHyNE Resource (NSF ECCS-2025633), the IIN, and Northwestern's MRSEC program (NSF DMR-1720139). Z.J. and A.M.R. acknowledge support from the U.S. Department of Energy (DOE), Office of Science, Office of Basic Energy Sciences, under grant number DE-SC0019281. A.K. (UPenn) acknowledges support from the National Science Foundation, under grant number DMR-1719353. The authors acknowledge computational support from the National Energy Research Scientific Computing Center (NERSC) of the DOE and the High-Performance Computing Modernization Office (HPCMO) of the U.S. Department of Defense (DOD). R.S.-Y. acknowledges the financial support from NSF DMR-1809439. K.K. and C.S. also acknowledge The Center for Nanoscale Materials (CNM) at Argonne National Laboratory (ANL), an Office of Science user facility, supported by the U.S. DOE, Office of Science, Office of Basic Energy Sciences, under Contract No. DE-AC02-06CH11357, where allowed to perform SEM analysis.

Conflict of Interest

The authors declare no conflict of interest.

Author Contributions

M.T.S. and A.K. contributed equally to this work. M.A. and A.K. (IIT) conceived the idea. A.K. (IIT) synthesized the nanostructured catalysts. A.K. (IIT), M.E., P.N.M.D., S.M., and J.H. performed the electrochemical experiment. A.K. (IIT) and M.E. did the XRD, XPS, Raman spectroscopy,

NMR, and in situ DEMS experiments. Z.J., performed the DFT calculations, A.K. (UPenn) helped with analyses and designing numerical experiments. A.M.R. supervised A.K. (UPenn) and Z.J. M.T.S. performed SEM, STEM, and EELS experiments. R.S.Y. supervised M.T.S. efforts. K.K. and C.S. performed SEM characterization. M.A. supervised A.K. (IIT), M.E., P.N.M.D., S.M., and J.H. efforts. All authors contributed to the manuscript before submission.

Keywords

lithium–air batteries, lithium–oxygen batteries, non-aqueous electrolytes, oxygen evolution reaction, transition metal phosphides

Received: June 12, 2020

Revised: October 3, 2020

Published online:

- [1] J. B. Varley, V. Viswanathan, J. K. Nørskov, A. C. Luntz, *Energy Environ. Sci.* **2014**, *7*, 720.
- [2] M. Park, H. Sun, H. Lee, J. Lee, J. Cho, *Adv. Energy Mater.* **2012**, *2*, 780.
- [3] R. Cao, J. S. Lee, M. Liu, J. Cho, *Adv. Energy Mater.* **2012**, *2*, 816.
- [4] Z. Xiang, D. Cao, L. Huang, J. Shui, M. Wang, L. Dai, *Adv. Mater.* **2014**, *26*, 3315.
- [5] J. Lu, Y. J. Lee, X. Luo, K. C. Lau, M. Asadi, H. H. Wang, S. Brombosz, J. Wen, D. Zhai, Z. Chen, D. J. Miller, Y. S. Jeong, J. B. Park, Z. Z. Fang, B. Kumar, A. Salehi-Khojin, Y. K. Sun, L. A. Curtiss, K. Amine, *Nature* **2016**, *529*, 377.
- [6] J. Xiao, D. Mei, X. Li, W. Xu, D. Wang, G. L. Graff, W. D. Bennett, Z. Nie, L. V. Saraf, I. A. Aksay, J. Liu, J. G. Zhang, *Nano Lett.* **2011**, *11*, 5071.
- [7] Y. C. Lu, Z. Xu, H. A. Gasteiger, S. Chen, K. Hamad-Schifferli, Y. Shao-Horn, *J. Am. Chem. Soc.* **2010**, *132*, 12170.
- [8] Z. Peng, S. A. Freunberger, Y. Chen, P. G. Bruce, *Science* **2012**, *337*, 563.
- [9] A. Débart, A. J. Paterson, J. Bao, P. G. Bruce, *Angew. Chem., Int. Ed.* **2008**, *47*, 4521.
- [10] Y. Cui, Z. Wen, Y. Liu, *Energy Environ. Sci.* **2011**, *4*, 4727.
- [11] S. Chen, J. Duan, M. Jaroniec, S. Z. Qiao, *Adv. Mater.* **2014**, *26*, 2925.
- [12] J. Kibsgaard, C. Tsai, K. Chan, J. D. Benck, J. K. Nørskov, F. Abild-Pedersen, T. F. Jaramillo, *Energy Environ. Sci.* **2015**, *8*, 3022.
- [13] L. Feng, H. Xue, *ChemElectroChem* **2017**, *4*, 20.
- [14] J. Kibsgaard, T. F. Jaramillo, *Angew. Chem., Int. Ed.* **2014**, *53*, 14433.
- [15] E. J. Popczun, J. R. McKone, C. G. Read, A. J. Biacchi, A. M. Wiltrot, N. S. Lewis, R. E. Schaak, *J. Am. Chem. Soc.* **2013**, *135*, 9267.
- [16] J. Xu, J. P. S. Sousa, N. E. Mordinova, J. D. Costa, D. Y. Petrovykh, K. Kovnir, O. I. Lebedev, Y. V. Kolen'ko, *ACS Catal.* **2018**, *8*, 2595.
- [17] X. Wang, Y. V. Kolen, X. Q. Ko, K. Bao, L. Kovnir, A. Liu, *Angew. Chem., Int. Ed. Engl.* **2015**, *54*, 8188.
- [18] K. U. D. Calvinho, A. B. Laursen, K. M. K. Yap, T. A. Goetjen, S. Hwang, N. Murali, B. Mejia-Sosa, A. Lubarski, K. M. Teeluck, E. S. Hall, E. Garfunkel, M. Greenblatt, G. C. Dismukes, *Energy Environ. Sci.* **2018**, *11*, 2550.
- [19] R. B. Wexler, J. M. P. Martirez, A. M. Rappe, *J. Am. Chem. Soc.* **2018**, *140*, 4678.
- [20] A. B. Laursen, R. B. Wexler, M. J. Whitaker, E. J. Izett, K. U. D. Calvinho, S. Hwang, R. Rucker, H. Wang, J. Li, E. Garfunkel, M. Greenblatt, A. M. Rappe, G. C. Dismukes, *ACS Catal.* **2018**, *8*, 4408.
- [21] A. Kondori, M. Esmaeilirad, A. Baskin, B. Song, J. Wei, W. Chen, C. U. Segre, R. Shahbazian-Yassar, D. Prendergast, M. Asadi, *Adv. Energy Mater.* **2019**, *9*, 1900516.
- [22] R. B. Wexler, J. M. P. Martirez, A. M. Rappe, *ACS Catal.* **2017**, *7*, 7718.
- [23] R. B. Wexler, J. M. P. Martirez, A. M. Rappe, *Chem. Mater.* **2016**, *28*, 5365.

- [24] M. W. Herdiech, A. Kakekhani, X. Zhu, S. Ismail-Beigi, E. I. Altman, *Surf. Sci.* **2019**, 688, 51.
- [25] S. Shaikhutdinov, *Catal. Lett.* **2018**, 148, 2627.
- [26] H. Abroshan, P. Bothra, S. Back, A. Kulkarni, J. K. Nørskov, S. Siahrostami, *J. Phys. Chem. C* **2018**, 122, 4783.
- [27] Z. Jiang, K. Klyukin, V. Alexandrov, *ACS Appl. Mater. Interfaces* **2018**, 10, 20621.
- [28] I. K. M. Yu, X. Xiong, D. C. W. Tsang, Y. H. Ng, J. H. Clark, J. Fan, S. Zhang, C. Hu, Y. S. Ok, *Green Chem.* **2019**, 21, 4341.
- [29] P. X. Wang, L. Shao, N. Q. Zhang, K. N. Sun, *J. Power Sources* **2016**, 325, 506.
- [30] S. Lee, G. H. Lee, H. J. Lee, M. A. Dar, D. W. Kim, *Sci. Rep.* **2017**, 7, 9495.
- [31] Q. Xu, X. Han, F. Ding, L. Zhang, L. Sang, X. Liu, Q. Xu, *J. Alloys Compd.* **2016**, 664, 750.
- [32] F. Li, D. M. Tang, Y. Chen, D. Golberg, H. Kitaura, T. Zhang, A. Yamada, H. Zhou, *Nano Lett.* **2013**, 13, 4702.
- [33] Y. Zhao, Y. Hang, Y. Zhang, Z. Wang, Y. Yao, X. He, C. Zhang, D. Zhang, *Electrochim. Acta* **2017**, 232, 296.
- [34] S. Ma, L. Sun, L. Cong, X. Gao, C. Yao, X. Guo, L. Tai, P. Mei, Y. Zeng, H. Xie, R. Wang, *J. Phys. Chem. C* **2013**, 117, 25890.
- [35] L. Zhang, X. Zhang, Z. Wang, J. Xu, D. Xu, L. Wang, *Chem. Commun.* **2012**, 48, 7598.
- [36] Y. J. Lee, S. H. Park, S. H. Kim, Y. Ko, K. Kang, Y. J. Lee, *ACS Catal.* **2018**, 8, 2923.
- [37] S. T. Kim, N. S. Choi, S. Park, J. Cho, *Adv. Energy Mater.* **2015**, 5, 1401030.
- [38] S. Ren, D. Joulié, D. Salvatore, K. Torbensen, M. Wang, M. Robert, C. P. Berlinguet, *Science* **2019**, 365, 367.
- [39] M. Esmaeilirad, A. Kondori, B. Song, A. Ruiz Belmonte, J. Wei, K. Kucuk, S. M. Khanvilkar, E. Efimoff, W. Chen, C. U. Segre, R. Shahbazian-Yassar, M. Asadi, *ACS Nano* **2020**, 14, 2099.
- [40] D. J. Lee, H. Lee, Y. J. Kim, J. K. Park, H. T. Kim, *Adv. Mater.* **2016**, 28, 857.
- [41] X. Gao, Y. Chen, L. Johnson, P. G. Bruce, *Nat. Mater.* **2016**, 15, 882.
- [42] B. J. Bergner, A. Schürmann, K. Peppler, A. Garsuch, J. Janek, *J. Am. Chem. Soc.* **2014**, 136, 15054.
- [43] B. J. Bergner, C. Hofmann, A. Schürmann, D. Schröder, K. Peppler, P. R. Schreiner, J. Janek, *Phys. Chem. Chem. Phys.* **2015**, 17, 31769.
- [44] H. D. Lim, B. Lee, Y. Zheng, J. Hong, J. Kim, H. Gwon, Y. Ko, M. Lee, K. Cho, K. Kang, *Nat. Energy* **2016**, 1, 16066.
- [45] X. Gao, Y. Chen, L. R. Johnson, Z. P. Jovanov, P. G. Bruce, *Nat. Energy* **2017**, 2, 31.
- [46] L. Johnson, C. Li, Z. Liu, Y. Chen, S. A. Freunberger, P. C. Ashok, B. B. Praveen, K. Dholakia, J. M. Tarascon, P. G. Bruce, *Nat. Chem.* **2014**, 6, 1091.
- [47] Y. Hou, J. Wang, J. Liu, C. Hou, Z. Xiu, Y. Fan, L. Zhao, Y. Zhai, H. Li, J. Zeng, X. Gao, S. Zhou, D. Li, Y. Li, F. Dang, K. Liang, P. Chen, C. Li, D. Zhao, B. Kong, *Adv. Energy Mater.* **2019**, 9, 1901751.
- [48] M. D. Radin, J. F. Rodriguez, F. Tian, D. J. Siegel, *J. Am. Chem. Soc.* **2012**, 134, 1093.
- [49] J. S. Hummelshøj, A. C. Luntz, J. K. Nørskov, *J. Chem. Phys.* **2013**, 138, 034703.
- [50] M. Asadi, B. Sayahpour, P. Abbasi, A. T. Ngo, K. Karis, J. R. Jokisaari, C. Liu, B. Narayanan, M. Gerard, P. Yasaei, X. Hu, A. Mukherjee, K. C. Lau, R. S. Assary, F. Khalili-Araghi, R. F. Kliewer, L. A. Curtiss, A. Salehi-Khojin, *Nature* **2018**, 555, 502.
- [51] M. Asadi, B. Kumar, C. Liu, P. Phillips, P. Yasaei, A. Behranginia, P. Zapol, R. F. Kliewer, L. A. Curtiss, A. Salehi-Khojin, *ACS Nano* **2016**, 10, 2167.
- [52] Y. Qiao, J. Yi, S. Guo, Y. Sun, S. Wu, X. Liu, S. Yang, P. He, H. Zhou, *Energy Environ. Sci.* **2018**, 11, 1211.
- [53] J. Yang, D. Zhai, H. H. Wang, K. C. Lau, J. A. Schlueter, P. Du, D. J. Myers, Y. K. Sun, L. A. Curtiss, K. Amine, *Phys. Chem. Chem. Phys.* **2013**, 15, 3764.
- [54] G. Rodríguez-Gattorno, A. Martínez-Hernández, L. O. Aleman-Vázquez, E. Torres-García, *Appl. Catal. A* **2007**, 321, 117.
- [55] C. Castillo, G. Buono-Core, C. Manzur, N. Yutronic, R. Sierpe, G. Cabello, B. Chornik, *J. Chil. Chem. Soc.* **2016**, 61, 2816.
- [56] N. S. McIntyre, D. D. Johnston, L. L. Coatsworth, R. D. Davidson, J. R. Brown, *Surf. Interface Anal.* **1990**, 15, 265.
- [57] F. Mizuno, S. Nakanishi, Y. Kotani, S. Yokoishi, I. Hideki, *Electrochemistry* **2010**, 78, 403.
- [58] Z. Zhao, J. Huang, Z. Peng, *Angew. Chem., Int. Ed.* **2018**, 57, 3874.
- [59] C. Ling, R. Zhang, K. Takechi, F. Mizuno, *J. Phys. Chem. C* **2014**, 118, 26591.
- [60] D. Zhai, K. C. Lau, H. H. Wang, J. Wen, D. J. Miller, J. Lu, F. Kang, B. Li, W. Yang, J. Gao, E. Indacochea, L. A. Curtiss, K. Amine, *Nano Lett.* **2015**, 15, 1041.
- [61] J. Lu, L. Cheng, K. C. Lau, E. Tyo, X. Luo, J. Wen, D. Miller, R. S. Assary, H. H. Wang, P. Redfern, H. Wu, J. B. Park, Y. K. Sun, S. Vajda, K. Amine, L. A. Curtiss, *Nat. Commun.* **2014**, 5, 5895.
- [62] C. Xia, C. Y. Kwok, L. F. Nazar, *Science* **2018**, 361, 777.
- [63] L. Cheng, P. Redfern, K. C. Lau, R. S. Assary, B. Narayanan, L. A. Curtiss, *J. Electrochem. Soc.* **2017**, 164, E3696.
- [64] M. J. Welland, K. C. Lau, P. C. Redfern, L. Liang, D. Zhai, D. Wolf, L. A. Curtiss, *J. Chem. Phys.* **2015**, 143, 224113.
- [65] A. Sun, K. Lv, D. Wang, Z. Wu, *Appl. Surf. Sci.* **2019**, 493, 740.
- [66] J. H. Du, H. Jin, Z. K. Zhang, D. D. Zhang, S. Jia, L. P. Ma, W. C. Ren, H. M. Cheng, P. L. Burn, *Nanoscale* **2017**, 9, 251.
- [67] F. Rahman, T. Ahmed, S. Walia, E. Mayes, S. Sriram, M. Bhaskaran, S. Balendhran, *Nanoscale* **2018**, 10, 19711.
- [68] S. Lu, Z. Qin, Q. Guo, G. Cao, *Appl. Surf. Sci.* **2017**, 392, 849.
- [69] B. Klingenbergs, F. Grellner, D. Borgmann, G. Wedler, *Surf. Sci.* **1997**, 383, 13.
- [70] D. Cappus, M. Haßel, E. Neuhaus, M. Heber, F. Rohr, H. J. Freund, *Surf. Sci.* **1995**, 337, 268.
- [71] C. Benndorf, H. Seidel, F. Thieme, *Surf. Sci.* **1977**, 67, 469.
- [72] W. Song, M. Yoshitake, *Appl. Surf. Sci.* **2005**, 251, 14.
- [73] S. Stuckenholz, C. Büchner, M. Heyde, H. J. Freund, *J. Phys. Chem. C* **2015**, 119, 12283.
- [74] P. Xiao, M. A. Sk, L. Thia, X. Ge, R. J. Lim, J. Y. Wang, K. H. Lim, X. Wang, *Energy Environ. Sci.* **2014**, 7, 2624.
- [75] J. S. Hummelshøj, J. Blomqvist, S. Datta, T. Vegge, J. Rossmeisl, K. S. Thygesen, A. C. Luntz, K. W. Jacobsen, J. K. Nørskov, *J. Chem. Phys.* **2010**, 132, 071101.
- [76] Y. Jing, Z. Zhou, *ACS Catal.* **2015**, 5, 4309.
- [77] J. K. Nørskov, J. Rossmeisl, A. Logadottir, L. Lindqvist, J. R. Kitchin, T. Bligaard, H. Jónsson, *J. Phys. Chem. B* **2004**, 108, 17886.
- [78] J. Rossmeisl, Z. W. Qu, H. Zhu, G. J. Kroes, J. K. Nørskov, *J. Electroanal. Chem.* **2007**, 607, 83.
- [79] M. D. Bhatt, J. Y. Lee, *J. Mol. Liq.* **2018**, 271, 274.
- [80] X. Zhang, A. Chen, M. Jiao, Z. Xie, Z. Zhou, *Batteries Supercaps* **2019**, 2, 498.
- [81] M. D. Radin, F. Tian, D. J. Siegel, *J. Mater. Sci.* **2012**, 47, 7564.
- [82] Z. Lyu, Y. Zhou, W. Dai, X. Cui, M. Lai, L. Wang, F. Huo, W. Huang, Z. Hu, W. Chen, *Chem. Soc. Rev.* **2017**, 46, 6046.
- [83] D. Aurbach, B. D. McCloskey, L. F. Nazar, P. G. Bruce, *Nat. Energy* **2016**, 1, 16128.
- [84] T. K. Zakharchenko, A. Y. Kozmenkova, D. M. Itkis, E. A. Goodilin, *Beilstein J. Nanotechnol.* **2013**, 4, 758.